Extraordinary Hall balance in ultrathin $SrRuO_3$ bilayers

van Thiel, T. C.; Groenendijk, D. J.; Caviglia, A. D.

DOI
10.1088/2515-7639/ab7a03

Publication date
2020

Document Version
Final published version

Published in
JPhys Materials

JPhys Materials

PAPER • OPEN ACCESS

Extraordinary Hall balance in ultrathin $SrRuO_3$ bilayers

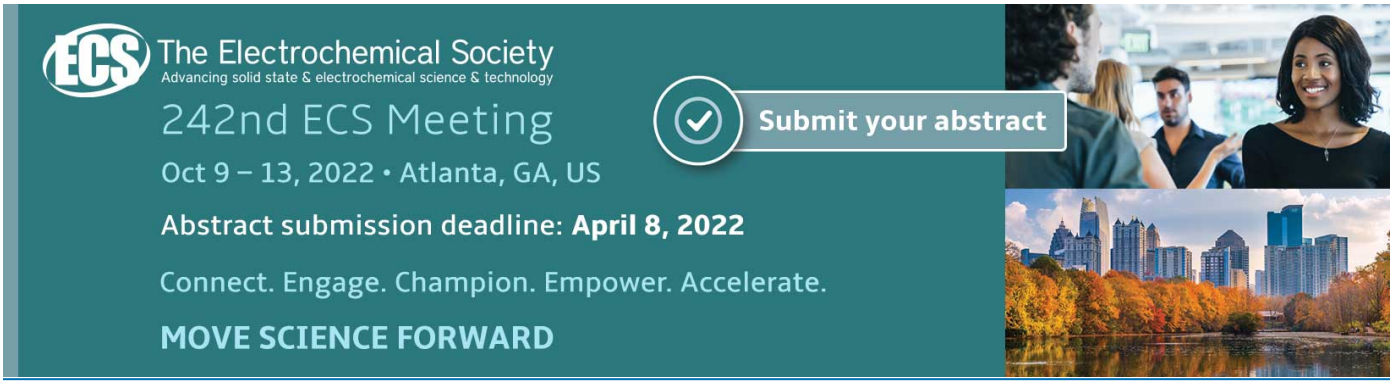

JPhys Materials

OPEN ACCESS

RECEIVED
16 December 2019

REVISED
13 February 2020

ACCEPTED FOR PUBLICATION
25 February 2020

PUBLISHED
17 March 2020

PAPER

Extraordinary Hall balance in ultrathin $SrRuO_3$ bilayers

T C van Thiel[1], **D J Groenendijk**[1] **and A D Caviglia**

Kavli Institute of Nanoscience, Delft University of Technology, Lorentzweg 1, 2628 CJ Delft, The Netherlands

[1] Equal contribution.

E-mail: a.caviglia@tudelft.nl

Keywords: oxide interfaces, spintronics, topological electronics

Supplementary material for this article is available online

Abstract

The correlated 4d transition metal oxide $SrRuO_3$ (SRO) features an anomalous Hall effect that originates from momentum-space sources of Berry curvature and depends sensitively on the magnetization. Here, we exploit this sensitivity and realize an epitaxial extraordinary Hall balance device, consisting of two ultrathin layers of SRO, separated by an insulating $SrTiO_3$ (STO) spacer. Our results highlight the potential of ultrathin SRO in the realization of oxide-based spintronic devices.

Introduction

Owing to its metallic properties, high chemical stability, and excellent compatibility with heteroepitaxy, $SrRuO_3$ (SRO) is a widely used material in oxide electronics [1–3]. One example is the synthesis of epitaxial supercapacitors, where two SRO electrode layers form atomically sharp interfaces with a high-k dielectric or ferroelectric material [4–8]. Another example is its use as a buffer layer in the growth of multiferroics [9, 10]. In addition to its suitability as an epitaxial electrode, its itinerant ferromagnetic ground state has attracted significant attention over the past years [11–13]. One aspect that has been intensively studied is its intriguing anomalous Hall effect (AHE), which originates from a source of Berry flux in momentum-space, also known as a magnetic monopole [14]. Acting like an effective magnetic field, the Berry flux causes electrons with opposite spins to experience opposing anomalous velocities, creating a voltage transverse to the longitudinally applied current [15, 16]. It was recently found that two-dimensional SRO is distinct from its three-dimensional counterpart as ultrathin films host not one, but multiple sources of Berry flux with distinct spin-orbital parity [17]. This translates to a topologically non-trivial character of bands at the Fermi level, which carry Chern numbers $\mathcal{C} = \pm 2$ and constitute positive and negative contributions to the anomalous Hall effect, respectively. The magnetization is an important parameter, as it shifts the two bands with respect to the Fermi energy, thereby controlling the sign and magnitude of the anomalous amplitude R_{xy}^{AH}. Manipulation of the AHE in ultrathin SRO has been demonstrated through various approaches, such as electrostatic gating and interface engineering [17–20].

An essential feature of ultrathin SRO is its thickness-driven metal–insulator transition, which occurs in the vicinity of 4 unit cells (u.c.) [21, 22]. As the thickness is decreased below this limit, confinement and structural effects deplete the density of states. This occurs simultaneously with a suppression of the Curie temperature and saturation magnetization. The thickness is therefore an effective tuning parameter for manipulating the AHE in ultrathin SRO and can be applied to realize spintronic devices. An application of this is the extraordinary Hall balance (EHB), which stacks two different ferromagnetic layers, creating a memory device with four states [23].

In this work, we synthesize a heterostructure consisting of two layers of ultrathin SRO, separated by an $SrTiO_3$ (STO) spacer. We tailor the SRO layer thicknesses such that they exhibit different magnetic properties, while retaining similar resistance values such that the current is divided roughly equally over the two layers. This results in an all-oxide EHB device that can be controlled by magnetic field and temperature. These results highlight the delicate nature of the AHE in ultrathin SRO and its potential in the realization of spintronic devices.

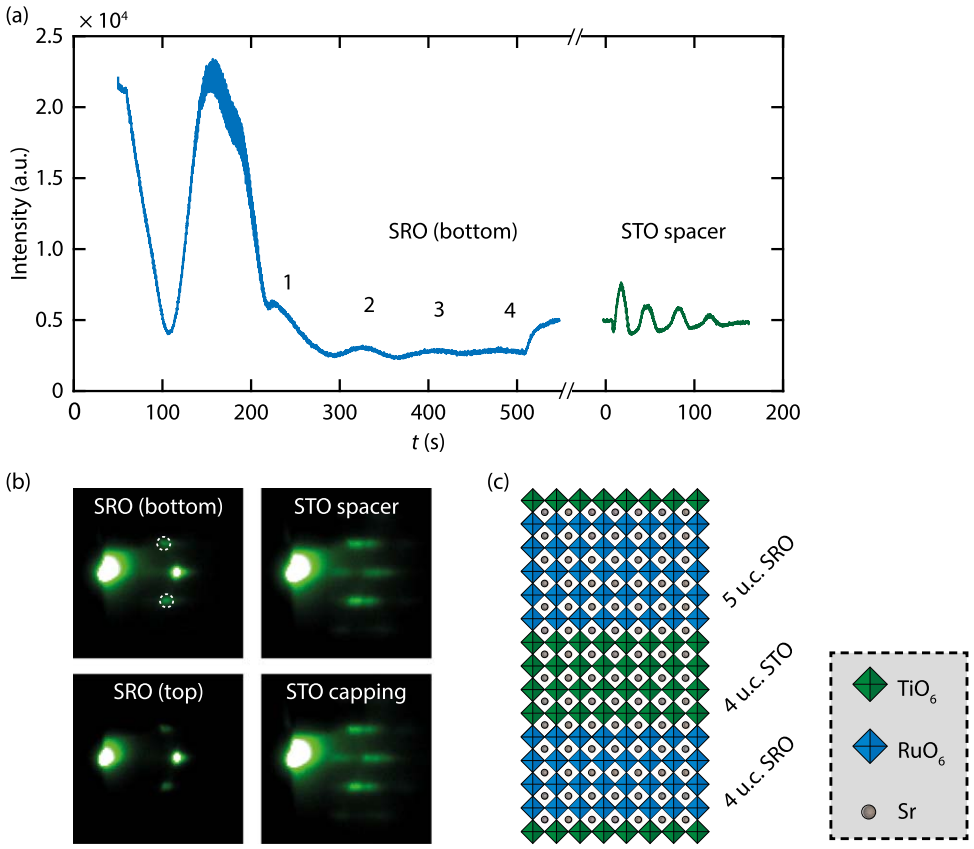

Figure 1. PLD synthesis. (a) RHEED intensity of the first-order diffraction spot during PLD growth of the first SRO and STO layers. (b) Post-growth RHEED patterns after each layer. (c) Illustration of the grown heterostructure, which consists of 4 u.c. SRO, 4 u.c. STO, 5 u.c. SRO and a 10 u.c. STO capping layer, grown on an STO substrate.

Results

Synthesis

The heterostructure is grown by pulsed laser deposition (PLD) and the growth is monitored by *in situ* reflection high-energy electron diffraction (RHEED). During the deposition, the intensity of the first-order diffraction spot is recorded. To realize the EHB device, we synthesize two layers of SRO, separated by a 4 u.c. (insulating) STO spacer. The SRO thicknesses are chosen to be 4 u.c. and 5 u.c. for the bottom and top layers, respectively. In figure 1(a), we show the RHEED intensity during growth of the bottom SRO layer. The initial oscillation is associated with a termination conversion from RuO_2 to SrO [24], which results in an enhancement of the surface diffusion of the ablated species. At the appropriate substrate temperature (~700°), this is usually followed by a step-flow growth mode, resulting in films with extremely low surface roughness [25]. A drawback however, is that it is more difficult to determine the number of layers grown due to the absence of layer-by-layer oscillations, particularly for substrates with large terrace widths [26]. We therefore opted for a slightly lower growth temperature (600°), for which RHEED oscillations are still faintly present. This allows for accurate determination of the layer thickness and growth rate, while maintaining a high surface quality. Discarding the initial oscillation [25], we stop the deposition at the fourth intensity maximum. We subsequently grow the 4 u.c. STO spacer, followed by the 5 u.c. SRO layer and finally a 10 u.c. protective STO capping layer. The RHEED patterns after completion of each layer are shown in figure 1(b). The well-defined spots of the SRO surfaces indicate that they are atomically smooth, whereas the slightly streaked spots of the STO surfaces are indicative of a shorther crystal coherence length compared to the SRO surfaces. Figure 1(c) shows an illustration of the SRO/STO/SRO heterostructure.

Transport

The longitudinal resistance of the heterostructure is shown as a function of temperature in figure 2(a). The derivative (dR/dT) is shown in the inset, where a sharp peak is observed at approximately 130 K. While a slight difference has been reported in the dR/dT behavior between bulk crystals and thin films [27–29], in both cases the peak is suggested to be caused by a logarithmic divergence of the specific heat due to short-range spin

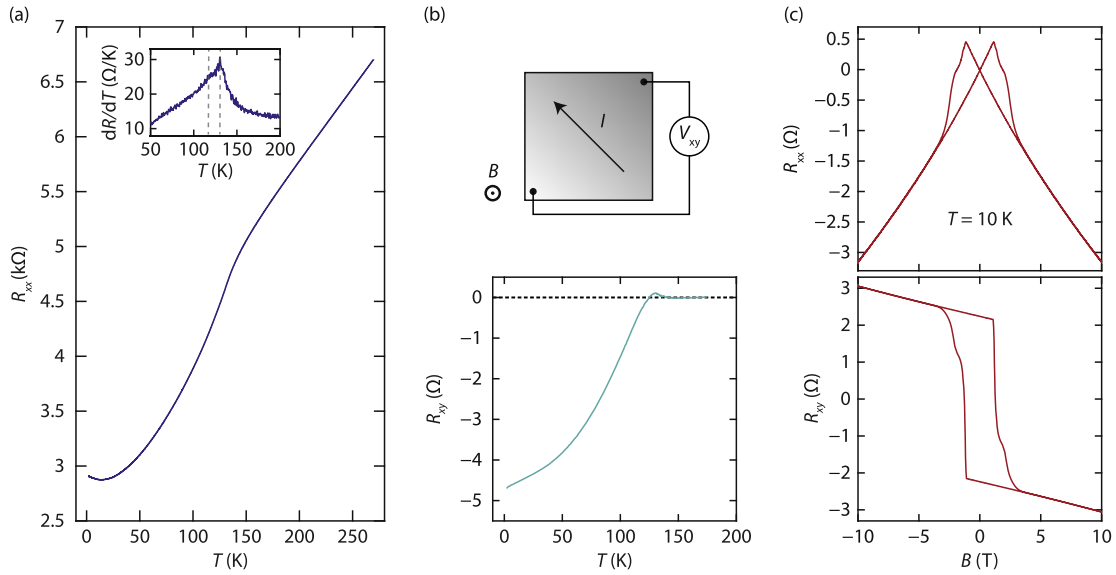

Figure 2. Magnetotransport. (a) Sheet resistance (R) versus temperature (T). The inset shows the derivative (dR/dT), with the gray dashed lines denoting the Curie temperatures of the two layers. (b) Top: schematic of the Hall measurement configuration. Bottom: magnitude of the AHE (R_{xy}^{AH}) as a function of temperature. (c) MR (top) and Hall resistance (bottom) as a function of temperature.

fluctuations across the magnetic phase transition [3, 30, 31]. As such, the peak at 130 K in the dR/dT identifies the Curie temperature of one of the SRO layers. Careful inspection reveals a shoulder at ∼115 K, identifying the magnetic phase transition of the second SRO layer. Considering the thickness-dependent suppression of T_c discussed prior, we attribute the high and low Curie temperatures to the 5 u.c. and 4 u.c. layers, respectively. This confirms a different temperature evolution of the magnetizations of the two layers, resulting in two distinct spin-polarized conduction channels. The temperature dependence of the Hall effect is shown in figure 2(b). The Hall resistance is measured in a four-point van der Pauw configuration, by cooling down while applying + and −50 mT (see the top panel of figure 2(b)). The applied fields ensure saturation of the magnetization upon cooling. Subsequent subtraction of the two curves and dividing by 2 removes the voltage offset originating from misalignment of the contacts and gives the total Hall resistance. This can be expressed as the sum of an anomalous and ordinary Hall component $R_{xy} = R_{xy}^{AH} + R_{xy}^{ord}$. Due to the high carrier density of SRO (∼10^{22} cm^{-3}), the ordinary Hall component for the ±50 mT fields is in the order of tens of mΩ and therefore much smaller than the anomalous component, which is in the order of several Ω. We can therefore neglect R_{xy}^{ord} such that $R_{xy} \simeq R_{xy}^{AH}$. At ∼120 K, we observe a sign change, which is characteristic of the intrinsic topological contribution to the AHE [17, 32]. This temperature corresponds to the magnetization value where the topological $\mathcal{C} = \pm 2$ bands compensate one another and the total anomalous amplitude is zero [17]. Above this temperature, the positive contribution dominates up until the Curie temperature, where the magnetization vanishes.

In figure 2(c), we show the magnetic field dependence of the (top) longitudinal (MR) and (bottom) Hall resistance. Both the MR and Hall data show that two magnetic transitions take place at different B_c. This provides a further indication of the presence of two spin-polarized conduction channels. From the Hall measurement we clearly recognize that the magnetization of one channel switches very abruptly, while that of the other channel switches more gradually. We attribute the channel that switches abruptly to the bottom SRO layer, as it is likely more ordered due to the growth on the atomically flat surface of the STO substrate. This is consistent with the abrupt switching observed for a single SRO layer. We expect the second SRO layer to be more disordered as it is grown on top of the SRO/STO stack, which has accumulated some surface roughness, as indicated by the RHEED patterns in figure 1. The concomitant variations in surface topography could give rise to magnetic domains with switching fields having a broader distribution than those of the bottom layer, resulting in a shallower slope at B_c.

For an EHB device, it is required that the two layers have different coercive fields. While this property has been established in figure 2(c), there are no field values at 10 K where the magnetic state is perfectly stable i.e. plateaus where $*R_{xy}^{AH} B \simeq 0$. We therefore proceed to study temperature dependent magnetic field sweeps to identify a regime where multiple magnetic states can be stabilized. A particularly interesting region is in the vicinity of the sign change observed in figure 2(b). Considering the different temperature evolutions of the two channels, it is likely that in this range, one channel exhibits a positive AHE while the other remains negative.

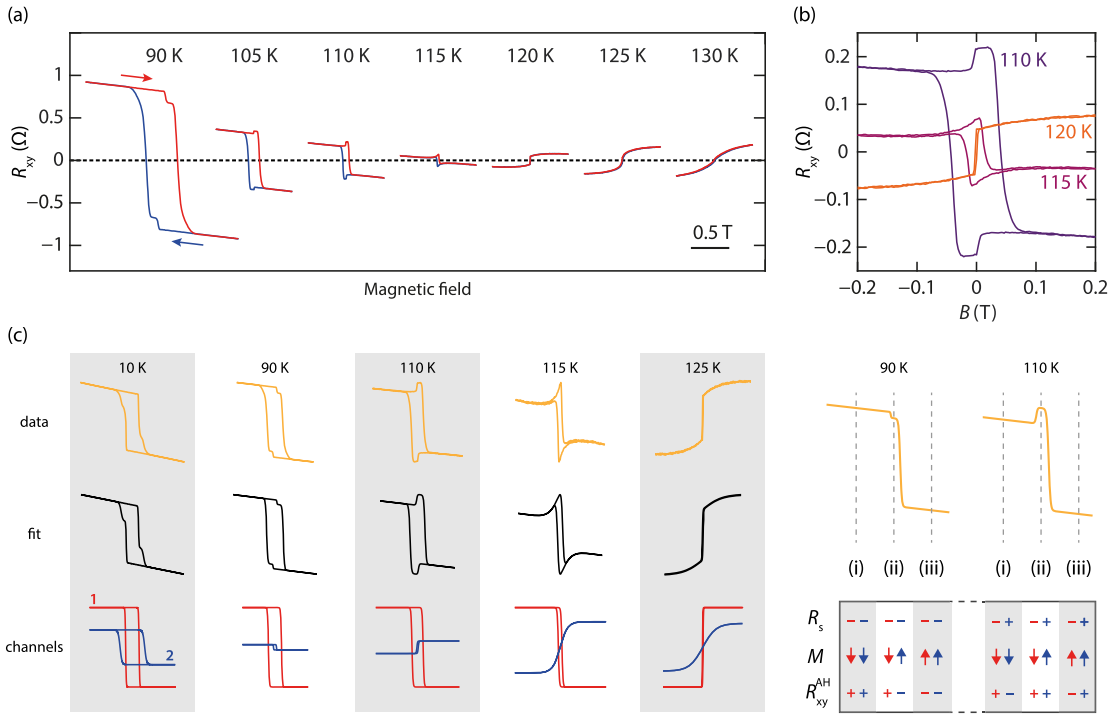

Figure 3. Temperature evolution. (a) AHE sweeps for various temperatures. The curves are offset horizontally for visual clarity. (b) Enlarged view of sweeps in the vicinity of the sign reversal temperature. (c) Left: disentanglement of the AHE data into two individual channels, labeled '1' (red) and '2' (blue). Right: The anomalous coefficient R_s, magnetization M and anomalous amplitude R_{xy}^{AH} at 90 and 110 K for the two channels along three points of the sweep. Arithmetic operators '+' and '–' denote the sign and the arrows denote the magnetization orientation.

Accordingly, we can expect a variety of different magnetic and electronic configurations. In figure 3(a), we show magnetic field sweeps in the temperature range 90 K $< T <$ 130 K. Figure 3(b) gives an enlarged view of sweeps recorded at 110, 115, and 120 K. In agreement with figure 2(b), we find that with increasing temperature, the overall sign of the AHE changes from negative to positive between 115 and 120 K. In addition, we find that for several temperatures—particularly for 90 and 110 K—three plateaus are present with a stable magnetic state. Remarkably, for 90 K the first plateau has a higher R_{xy} value than the second plateau, whereas the situation is inverted at 110 K. To gain more insight in the behavior of the two channels, it is necessary to separate the signal into its two individual components. We first remark that in general, two Hall resistances cannot be added to give the total Hall resistivity. However, it can be shown (see the supplementary information available online at stacks.iop.org/JPMATER/3/025005/mmedia) that in the small Hall angle limit ($R_{xy} \ll R_{xx}$), the summation of two Hall channels R_{xy}^{a} and R_{xy}^{b} is given by

$$R_{xy}^{tot} \simeq \left(\frac{R_{xx}^{tot}}{R_{xx}^{a}}\right)^2 R_{xy}^{a} + \left(\frac{R_{xx}^{tot}}{R_{xx}^{b}}\right)^2 R_{xy}^{b} \tag{1}$$

i.e. the two resistances (voltages) are scaled by the fraction of the total current they carry. Since in ultrathin SRO films the longitudinal resistance is about three orders of magnitude larger than the Hall resistance, this expression is valid and the total Hall resistance is a linear sum of the two individual channels. Using the empirical relation [14] $R_{xy}^{AH} = R_s M_z$, this allows us to introduce the following phenomenological model

$$R_{xy}^{AH,tot} = R_s^{a} M_z^{a} + R_s^{b} M_z^{b}, \tag{2a}$$

$$= R_s^{a} \tanh[\omega^{a}(B - B_c^{a})] + R_s^{b} \tanh[\omega^{b}(B - B_c^{b})], \tag{2b}$$

where R_s is the anomalous Hall coefficient, M_z the out-of-plane component of the magnetization, B_c the coercive field and ω a parameter describing the slope at $B = B_c$. The hyperbolic tangent models the switching of the magnetization at the coercive field. For simplicity, we have assumed the current fractions to be approximately equal and absorb the scaling factor into R_s. Fitting equation (2b) to the experimental data allows us to simulate the AHE of the two individual channels. The results are shown in the left panel of figure 3(c). The top row shows the measured R_{xy}, while the middle and bottom rows show simulated AH curves. The blue and red curves (bottom row) are the individual AH channels used for the simulation. The ordinary Hall component is taken into account through a linear fit at high field. Note that both the width (B_c) and the height (R_{xy}^{AH}) of the hysteresis loops in this figure are rescaled for visual clarity. The simulated curves provide an excellent description of the

experimentally observed behavior. Both AH components show a sign change, as well as a decrease of B_c with increasing temperature, consistent with the behavior of single SRO layers. Channel 1 (red) changes sign at ~100 K and channel 2 (blue) at ~120 K. Additionally, the coercive fields of the two channels are well separated, which is essential for an EHB device. This further confirms the different temperature evolution of the magnetization in figure 2(a). In the right panel of figure 3(c), we illustrate the EHB functionality of the heterostructure for 90 and 110 K, where stable plateaus are observed. The three different magnetic states of the forward sweeps $B < B_{c,2} < B_{c,1}$, $B_{c,2} < B < B_{c,1}$ and $B_{c,2} < B_{c,1} < B$ are labeled (i), (ii) and (iii), respectively. The table below summarizes the signs of the anomalous coefficients (R_s), the orientation of the magnetization (M) and the resulting AHE amplitude (R_{xy}^{AH}) for channels 1 and 2 (red and blue). The key difference between the two temperatures is the sign of channel 2, which is negative at 90 K, but positive at 110 K. This causes the different behavior in state (ii) between the two temperatures, resulting in a step down of R_{xy}^{AH} at 90 K, but a step up at 110 K. As a result, the EHB properties can be controlled with temperature, which adds a tuning parameter to the device.

Conclusion

The sensitive relationship between the AHE and the layer thickness in ultrathin SRO is a powerful element in synthesizing films with tailored properties. By controlling the thickness on an atomic scale, this sensitivity can be harnessed and the AHE can be controlled. We demonstrated this by creating an all-oxide EHB device, consisting solely out of two separated SRO layers with slightly different thicknesses. We further showed that, due to the intrinsic sign change of the AHE in SRO, the EHB functionality can be controlled by temperature. These results highlight the delicate nature of the AHE in SRO, as well as its potential for application in spintronic devices.

Additional information

Methods

The heterostructure was grown on a TiO_2-terminated $SrTiO_3$ substrate. The deposition was done by PLD, using a 248 nm KrF excimer laser at a 1 Hz repetition rate and a laser fluence of 1.7 J cm^{-2}. The growth temperature and pressure were 600 °C and 0.1 mbar O_2, respectively. The sample was capped by a 10 u.c. crystalline STO layer to impose symmetric boundary conditions [17] and to prevent degradation due to exposure to ambient conditions [33]. Heating is performed with an infrared diode laser. The temperature was measured with a pyrometer and the growth is monitored with *in situ* RHEED. After growth, the sample was annealed for 1 h in 300 mbar O_2 at 550°, minimizing the oxygen vacancies that might have formed, and subsequently cooled down to room temperature at 20 °C min^{-1} in the same pressure. Transport measurements were performed in an Oxford flow cryostat with a base temperature of 1.5 K and equipped with a 10 T superconducting magnet. Ohmic contacts to the the two SRO layers were established by ultrasonic Al wedge bonding. A ~15 Hz 10 μA current was sourced in a four-point van der Pauw geometry and the resulting longitudinal and transverse voltages were measured with a lock-in amplifier. Longitudinal and transverse resistances were subsequently obtained by dividing by the current.

Acknowledgments

The authors thank M Cuoco, C Autieri and W Brzezicki for fruitful discussions. This work was supported by the European Research Council under the European Unions Horizon 2020 programme/ERC Grant Agreements Nos. [677458] (Altermateria) and [731473] (Quantox of QuantERA ERA-NET Cofund in Quantum Technologies) and by the Netherlands Organisation for Scientific Research (NWO/OCW) as part of the Frontiers of Nanoscience program (NanoFront) and VIDI program.

ORCID iDs

T C van Thiel https://orcid.org/0000-0003-4396-5227
A D Caviglia https://orcid.org/0000-0001-9650-3371

References

[1] Eom C, Van Dover R, Phillips J M, Werder D, Marshall J, Chen C, Cava R J, Fleming R and Fork D 1993 *Appl. Phys. Lett.* **63** 2570
[2] Liu K-S, Tseng T-F and Lin I-N 1998 *Appl. Phys. Lett.* **72** 1182
[3] Koster G, Klein L, Siemons W, Rijnders G, Dodge J S, Eom C-B, Blank D H and Beasley M R 2012 *Rev. Mod. Phys.* **84** 253

[4] Izuha M, Abe K and Fukushima N 1997 *Japan. J. Appl. Phys.* **36** 5866
[5] Lin J, Natori K, Fukuzumi Y, Izuha M, Tsunoda K, Eguchi K, Hieda K and Matsunaga D 2000 *Appl. Phys. Lett.* **76** 2430
[6] Wohlfahrt-Mehrens M, Schenk J, Wilde P, Abdelmula E, Axmann P and Garche J 2002 *J. Power Sources* **105** 182
[7] Kim D, Jo J, Kim Y, Chang Y, Lee J, Yoon J-G, Song T and Noh T 2005 *Phys. Rev. Lett.* **95** 237602
[8] Shin Y J *et al* 2017 *Adv. Mater.* **29** 1602795
[9] Zheng R, Gao X, Wang J and Ramakrishna S 2008 *J. Am. Ceram. Soc.* **91** 463
[10] Wu J and Wang J 2009 *J. Appl. Phys.* **106** 054115
[11] Dodge J *et al* 1999 *Phys. Rev.* B **60** R6987
[12] Jeong D *et al* 2013 *Phys. Rev. Lett.* **110** 247202
[13] Kim M and Min B 2015 *Phys. Rev.* B **91** 205116
[14] Fang Z, Nagaosa N, Takahashi K S, Asamitsu A, Mathieu R, Ogasawara T, Yamada H, Kawasaki M, Tokura Y and Terakura K 2003 *Science* **302** 92
[15] Karplus R and Luttinger J 1954 *Phys. Rev.* **95** 1154
[16] Nagaosa N, Sinova J, Onoda S, MacDonald A and Ong N 2010 *Rev. Mod. Phys.* **82** 1539
[17] Groenendijk D J *et al* 2018 arXiv:1810.05619
[18] Shimizu S, Takahashi K S, Kubota M, Kawasaki M, Tokura Y and Iwasa Y 2014 *Appl. Phys. Lett.* **105** 163509
[19] Mizuno H, Yamada K T, Kan D, Moriyama T, Shimakawa Y and Ono T 2017 *Phys. Rev.* B **96** 214422
[20] Ohuchi Y, Matsuno J, Ogawa N, Kozuka Y, Uchida M, Tokura Y and Kawasaki M 2018 *Nat. Commun.* **9** 213
[21] Chang Y J, Kim C H, Phark S-H, Kim Y, Yu J and Noh T 2009 *Phys. Rev. Lett.* **103** 057201
[22] Xia J, Siemons W, Koster G, Beasley M and Kapitulnik A 2009 *Phys. Rev.* B **79** 140407
[23] Zhang S, Liu Y, Collins-McIntyre L, Hesjedal T, Zhang J, Wang S and Yu G 2013 *Sci. Rep.* **3** 2087
[24] Rijnders G, Blank D H, Choi J and Eom C-B 2004 *Appl. Phys. Lett.* **84** 505
[25] Choi J, Eom C-B, Rijnders G, Rogalla H and Blank D H 2001 *Appl. Phys. Lett.* **79** 1447
[26] Hong W, Lee H N, Yoon M, Christen H M, Lowndes D H, Suo Z and Zhang Z 2005 *Phys. Rev. Lett.* **95** 095501
[27] Klein L, Dodge J, Ahn C, Snyder G, Geballe T, Beasley M and Kapitulnik A 1996 *Phys. Rev. Lett.* **77** 2774
[28] Roussev R and Millis A 2000 *Phys. Rev. Lett.* **84** 2279
[29] Klein L, Dodge J, Geballe T, Beasley M and Kapitulnik A 2000 *Phys. Rev. Lett.* **84** 2280
[30] Fisher M E and Langer J 1968 *Phys. Rev. Lett.* **20** 665
[31] Alexander S, Helman J and Balberg I 1976 *Phys. Rev.* B **13** 304
[32] Fang C, Lu L, Liu J and Fu L 2016 *Nat. Phys.* **12** 936
[33] Groenendijk D, Manca N, Mattoni G, Kootstra L, Gariglio S, Huang Y, van Heumen E and Caviglia A 2016 *Appl. Phys. Lett.* **109** 041906